

DFT Studies of the Structure and Vibrational Spectra of Isolated Molybdena Species Supported on Silica

Shaji Chempath, Yihua Zhang, and Alexis T. Bell*

Department of Chemical Engineering, University of California, Berkeley, Berkeley, California 94720-1462

Received: July 25, 2006; In Final Form: October 10, 2006

Different cluster models of isolated Mo^{VI} molybdate species anchored on silica surface were investigated using density functional theory (DFT). Isolated molybdate centers were modeled as either a penta-coordinated mono-oxo species or a tetra-coordinated di-oxo species. Standard free energy changes for interconversion between mono-oxo and di-oxo species indicate that these two species can coexist in equilibrium on the surface of amorphous silica with di-oxo species being the favored species at high temperature and low partial pressures of water. Comparison of Raman-spectra from experiment and DFT suggests that di-oxo species might be the prominent species responsible for the peak at 988 cm⁻¹. This conclusion is strongly supported by the similarity in the EXAFS spectra obtained from experiment and theory. The thermodynamics for H₂ reduction of isolated molybdate species were determined and found to be in reasonable agreement with experimental observation. DFT calculations of the structure and properties of the reduced Mo^{IV} centers and comparison of these with experimental results suggest that the reduced centers are present as mono-oxo species.

Introduction

Dispersed molybdena (MoO_x) catalysts are active for a variety of reactions, including olefin metathesis,^{1,2} selective oxidation reactions,^{3–5} the oxidative dehydrogenation of low molecular weight alkanes,⁶ the oxidation of NH₃,^{7,8} and the selective catalytic reduction of NO by NH₃.⁹ These and other studies have also shown that the reactivity of supported MoO_x catalysts is dependent on the structure of the dispersed MoO_x^{4,10,11} and that, depending on the Mo surface concentration, Mo may be present as isolated monomolybdate units, polymolybdate domains, and MoO₃ crystallites.¹² The coexistence of multiple Mo structures makes it difficult to isolate the relationship of the molybdate structure and catalytic activity and selectivity. This constraint is eliminated for very low Mo surface coverage (<1 Mo/nm²), where virtually all of the Mo is present as isolated monomolybdate species.

The structural characterization of isolated molybdate species dispersed on an oxide support (e.g., silica, alumina, and titania) has been the subject of considerable research.^{10–21} A primary question is whether the surface bonded molybdate species take on a penta-coordinated, square pyramidal structure containing one Mo=O bond or a tetrahedral structure containing two Mo=O bonds. Precedents exist for both types of structures, often referred to as mono-oxo and di-oxo species, in mono-nuclear molybdate compounds.^{22–24} For example, mono-oxo structures are exemplified by MoOF₄ and MoO(OSi(O-^tBu)₃)₄ and di-oxo structures, by MoO₂Cl₂ and MoO₂(OSi(O-^tBu)₃)₂. Attempts to make a definitive statement about the structure of highly dispersed molybdate species have been difficult because the structure of the dispersed species can depend on the properties of the support (i.e., the degree of hydroxylation), the nature of the Mo precursor, and the conditions of calcinations following dispersion of the Mo precursor.

The characterization of isolated molybdate species dispersed on silica has received particular attention because the support

is irreducible and relatively inert.^{15–21,25–27} While evidence for di-oxo species has been presented based on information obtained from EXAFS, NEXAFS, ESR, UV–visible spectroscopy, and Raman spectroscopy, the presence of mono-oxo species could not be excluded.^{15,17,19,27} It is also noted that some investigators have argued in favor of mono-oxo species based on the failure to observe more than two bands in the Raman spectrum of isolated molybdate species that had been partially exchanged with ¹⁸O.^{15,17,27} There have also been several attempts made to represent the structure of molybdate species on silica; however, the models used to describe the silica surface were very simple and the theoretical methods used were not validated for their accuracy.^{19,28,29}

The objective of this study was to develop and validate a model for mono-oxo and di-oxo molybdate species supported on the surface of amorphous silica. To this end, density functional theory (DFT) was used to calculate the structure, vibrational frequencies, and relative stability of isolated molybdate species anchored to different cluster representations of the surface of amorphous silica. A further objective of the work was to determine the thermodynamics for reducing Mo^{VI} species to Mo^{IV} species, since this process has been proposed to occur during the oxidation of methane to formaldehyde over isolated molybdate species dispersed on silica. The structures calculated in the present study were then compared with XANES, EXAFS, and Raman data reported recently for highly dispersed MoO_x on silica.²⁷

Methods

Electronic energies of reactant, product, and transition states were determined using density functional theory (DFT). The B3LYP functional was used to describe electron exchange and correlation, and the 6-31G* basis set was used to locate optimized ground-state and transition-state structures. The LANL2DZ effective core potential was used to describe the Mo atom. Mono-oxo and di-oxo molybdate species bonded to

* Corresponding author. E-mail: bell@cchem.berkeley.edu.

TABLE 1: Calculated and Experimentally Observed Bond Lengths and Bond Angles for MoO₂Cl₂ and MoF₄

		EXPT ref 23	DFT (B3LYP/6-31G*)
MoO ₂ Cl ₂	Mo=O	1.687 Å	1.695 Å
	Mo–Cl	2.255 Å	2.273 Å
	O=Mo=O	106.3°	106.7°
	Cl–Mo–Cl	113.9°	112.2°
	O=Mo–Cl	109.7°	109.5°
		EXPT ref 22	DFT (B3LYP/6-31G*)
MoOF ₄	Mo=O	1.836 Å	1.850 Å
	Mo–F	1.650 Å	1.673 Å
	O=Mo–F	103.8°	105.3°
	F–Mo–F	86.7°	86.0°

silica were treated as free-standing clusters. The Si atoms at the boundary of the cluster were terminated by H atoms. All of the atoms in the cluster were allowed to relax during the geometry optimizations, which were done using the Gaussian03 software.³⁰ Vibrational frequencies were calculated at the B3LYP/6-31G* level and were scaled by a factor of 0.961.³¹ Molden,³² a freeware, was used for visualization of the geometries and vibrational frequencies. After a particular molecular structure was optimized to a stationary point (transition state, or minimum energy structure), its energy was further refined by a calculation at a higher level of accuracy using the LACV3P**++ basis set, as implemented in the Jaguar software.³³ Molybdenum was treated using effective core potentials within the LACV3P**++ basis set.

Free energies of all structures were determined within the rigid-rotor, harmonic-oscillator approximation. The Hessian matrix required for such calculations was evaluated analytically by the Gaussian 03 software with the 6-31G*/LANL2DZ basis set. Standard free energies were calculated by including translational, rotational, and vibrational partition functions. In reporting the energy change of reactions, the symbol ΔE is used to denote the change in electronic energy with the zero-point corrections and the symbol ΔG^0 is used to denote the standard change in free energy of reaction at 920 K, the temperature at which methane oxidation to formaldehyde was carried out experimentally.³⁴ The standard state for all species present in the gas phase was taken to be 1 atm. The standard state for molybdena species on the catalyst surface was taken to be a mole fraction of 1 (normalized by the total amount of molybdenum present). It should be noted, though, that the choice of standard state for surface species does not affect the values of ΔG^0 reported here, since all of the reactions considered have equal numbers of surface species in the reactant and product states. Therefore, the contribution to the standard free energy from the standard state density term cancels out when ΔG^0 is calculated as the difference between the reactant and product free energies.

Results and Discussion

Validation of Theoretical Approach. The theoretical methods used in this study were validated by comparing the calculated geometries and vibrational frequencies of MoOF₄ and MoO₂Cl₂ with those observed experimentally. MoOF₄ has a square pyramidal, mono-oxo structure, whereas MoO₂Cl₂ has a tetrahedral, di-oxo, structure.^{22,23} Table 1 lists both the calculated and observed bond distances and bond angles for both compounds. The agreement between theory and experiment is quite good for both model compounds.

The calculated and experimentally observed Mo=O stretching frequencies for both model compounds are listed in Table 2.

TABLE 2: Calculated and Experimentally Observed Vibrational Frequencies for MoO₂Cl₂ and MoF₄

		EXPT ^a	6-31G* scaled by 0.961	LACV3P**++ without scaling
MoOF ₄	Mo=O	1048	1044	1036
	Mo–F	714	711	683
MoO ₂ Cl ₂	(O=Mo=O) _{sym}	997	991	994
	(O=Mo=O) _{asym}	971	975	965
	(Cl–Mo–Cl) _{sym}	434	398	399
	(Cl–Mo–Cl) _{asym}	450	408	413

^a Experimental values for MoOF₄ and MoO₂Cl₂ are from refs 35 and 36 respectively.

Since vibrational frequencies obtained from DFT calculations are usually higher than those observed experimentally, the calculated values were multiplied by 0.961, as is recommended for the B3LYP/6-31G* level density functional theory.³¹ Good agreement is observed between theory and experiment^{35,36} for both model compounds. Therefore, a scaling factor of 0.961 was used for all subsequent calculations when reporting the vibrational frequencies for the B3LYP/6-31G*/LANL2DZ level of theory. Vibrational analysis of MoO₂Cl₂ and MoOF₆, using the larger LACV3P**++ basis set predicts frequencies close to the experimental values without scaling (see Table 2). However, the computational cost of carrying out a vibrational analysis using such a large basis set for molecules with more than 10 atoms is too high to justify using this level of theory.

Structures of Isolated Silica-Supported MoOx Species.

Three different models for the silica surface are shown in Figure 1. The first two models are formed by “cutting” small clusters of atoms from the surface of crystalline cristoballite. The first model, referred to as silica-100, is formed by taking seven silicon atoms from the crystallographic positions of 100 surface of cristoballite. The Accelrys MS modeling software³⁷ was used to represent the 100 surface of cristoballite and define the positions of the seven silicon atoms and the associated oxygen atoms. The Si–O bonds of the cluster that lie inside the crystal are saturated by hydrogen atoms (as Si–H). These terminating hydrogen atoms are not shown in Figure 1 for clarity. The surface Si–O bonds are terminated by forming silanol (Si–OH) groups. A similar procedure was used to define a silica-111 model for the 111 surface of cristoballite. The third model was constructed by forming a four-membered ring in which each Si atom is bonded to two other Si atoms by Si–O– bonds and is terminated by two silanol Si–OH groups. This model was constructed so that a mono-oxo species could be attached to

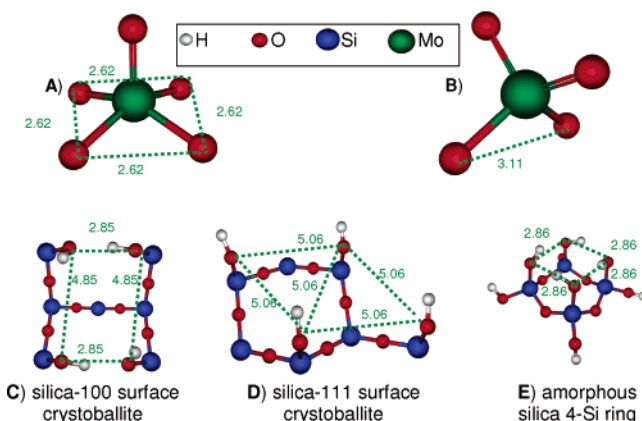


Figure 1. Coordination shell of Mo^{VI} in the mono-oxo (A) and di-oxo (B) forms and models for the silica surface before attaching molybdena (C–E).

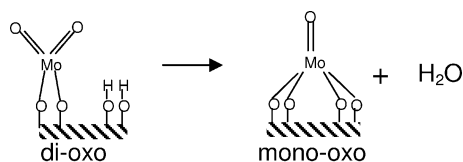
TABLE 3: Calculated Values of ΔE , $\Delta G^0(920)$, and $K(920)$ for Converting di-oxo to mono-oxo Molybdate Species with the Release of a Water Molecule

surface	ΔE , kcal/mol	$\Delta G^0(920)$, kcal/mol	$K(920)$
4 silica ring	21.3	5.9	0.040
silica-100	5.4	-28.0	4.5×10^6
silica-111	5.8	-17.1	1.2×10^4

the top of the structure. This model will be referred to as a 4-Si ring. Since molecular dynamics simulations of amorphous silica suggest that rings containing two to seven silicon atoms are present on the surface of amorphous silica,³⁸ all three arrangements mentioned above are considered to be reasonable physically. Other arrangements such as five-membered or six-membered rings may also be present on the surface; however, only the three models noted were considered, since they are suitable for anchoring isolated molybdate species.

Structures **A** and **B** in Figure 1 represent typical coordination spheres for Mo^{VI} in mono-oxo and di-oxo forms. These structures were obtained by geometry optimization of the model compounds $((\text{HO})_3\text{SiO})_4\text{MoO}$ and $((\text{HO}_3)\text{SiO})_2\text{Mo}(\text{O})_2$ using DFT. The mono-oxo species has four oxygen atoms lying in a plane at the corners of a 2.62 Å square. In order to anchor such a species on the surface of silica, there should be four silanol groups arranged in a similar square geometry. As shown in Figure 1 structure **E** has four such OH groups separated by 2.86 angstroms on the surface of the 4-Si ring. Similar sets of four hydroxyl groups do not appear, though, on silica-100 or silica-111, structures **C** and **D**. Thus adding a mono-oxo species and forming four Mo–O–Si bonds on these surfaces is expected to result in substantial strain of the silica surface. However, the di-oxo species will fit well on any of the surfaces because only two Mo–O–Si bonds need to be made with the silica surface. On the basis of such qualitative arguments, we expect mono-oxo species to be stabilized on 4-Si ring.

The conversion of di-oxo to mono-oxo molybdate species can occur in two ways. The first involves the release of a water molecule, as shown below:



Reaction 1

The calculated energy and free energy changes for reaction 1 occurring on different surface models are given in Table 3. Relevant bond angles and bond lengths are summarized in Table 4. The structures of mono-oxo and di-oxo species on a 4-Si ring are shown in Figure 2 as structures **F** and **G**. The corresponding structures for silica-100 and silica-111 are given in the Supporting Information. The value of ΔE for converting a di-oxo to mono-oxo species bonded to the 4-Si ring is 21.3 kcal/mol, whereas the values of ΔE for the same reaction occurring on the silica-100 and silica-111 surface structures are 5.4 and 5.8 kcal/mol, respectively. Therefore, although we had initially expected mono-oxo species to be stabilized on the 4-Si ring based on simple geometric arguments, the calculated values of ΔE indicate that mono-oxo species are better stabilized on the other two surface models. This can be explained as follows. Examination of Table 4 shows that the Mo–O–Si bond angles are substantially smaller for mono-oxo species attached to a 4-Si ring compared to the Mo–O–Si angles determined for

TABLE 4: Bond Lengths and Bond Angles of mono-oxo and di-oxo Mo Species on the Three Models of the Surface of Amorphous Silica

		4-Si	silica-100	silica-111
mono-oxo	Mo=O	1.69 Å	1.69 Å	1.69 Å
	Mo–O ^a	1.94 Å	1.92 Å	1.92 Å
	Mo–O–Si ^a	119°	149°	145°
	O=Mo–O ^a	109°	108°	105°
di-oxo	Mo=O ^a	1.71 Å	1.71 Å	1.71 Å
	Mo–O ^a	1.90 Å	1.91 Å	1.88 Å
	Mo–O–Si ^a	130°	133°	143°
	O=Mo–O ^a	115°	110°	109°
	O=Mo=O	107°	107°	109°

^a In the case of multiple angles or bond lengths the values reported are averages over equivalent bond angles or lengths. For example the Mo–O bond length listed for mono-oxo species is the average of the four Mo–O bonds in this structure.

the other two surface models. The rigid nature of the 4-Si ring forces the Mo–O–Si bond angle to be 119°, whereas the other two surfaces are more flexible and allow the Mo–O–Si angle to be in the range of 140–145°. Calculations for model compounds such as $((\text{HO})_3\text{SiO})_4\text{MoO}$ and $((\text{HO}_3)\text{SiO})_2\text{Mo}(\text{O})_2$ give the Mo–O–Si bond angle in the range of 140–150°. Thus, the bending of the four Mo–O–Si bond angles to 119° explains the higher ΔE for forming the mono-oxo species on the 4-Si ring. It is notable that the ΔE for converting the di-oxo species to mono-oxo is positive for all three models of the silica surface, which suggests that the silica surface undergoes some strain to accommodate four Mo–O–Si linkages. In the case of the silica-100 and silica-111 surfaces, the present calculations may

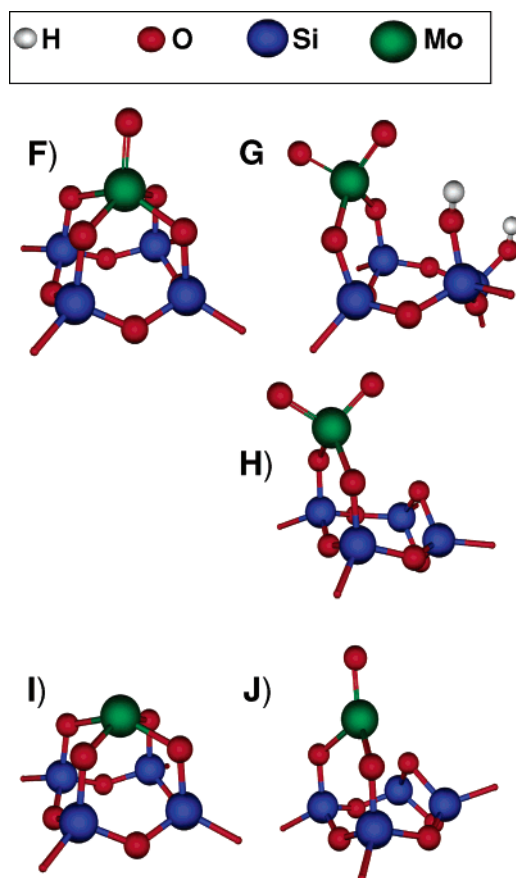
**Figure 2.** Geometry-optimized structures of molybdate species attached to the 4-silica ring: (F) mono-oxo Mo^{VI} ; (G) di-oxo Mo^{VI} with silanol groups; (H) di-oxo Mo^{VI} species without silanol groups; (I) reduced species Mo^{IV} ; (J) reduced species Mo^{IV} with an oxo group.

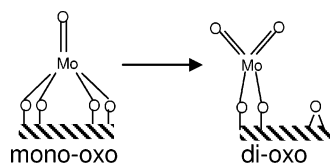
TABLE 5: Calculated Values of ΔE , $\Delta G^0(920)$, and $K(920)$ for Converting mono-oxo to di-oxo Molybdate Species with the Formation of Additional Si–O–Si Linkages on the Surface of Silica.

surface	ΔE , kcal/mol	$\Delta G^0(920)$, kcal/mol	$K(920)$
4 silica ring	11.7	−0.2	1.12
silica-100	−4.1	−13.2	1367
silica-111	−1.7	−6.0	26.6

underestimate the contribution of strain, since the silica cluster has been terminated by Si–H bonds and all of the atoms are allowed to relax during optimization of the geometry. In reality, there are Si–O–Si bonds at the boundaries which may have to undergo substantial rearrangement to accommodate the four Mo–O–Si links when a mono-oxo species is formed. When three of the terminating hydrogen atoms in the silica-111 model were held fixed, the value of ΔE for converting di-oxo to mono-oxo species increased from 5.8 to 19.0 kcal/mol. Since we are primarily concerned with amorphous silica, a flexible model of the surface is appropriate and the atoms at the boundary should be allowed to relax during geometry optimization.

The conversion of di-oxo to mono-oxo species as denoted by Reaction 1 leads to the release of a water molecule into the gas phase and is, hence, favored entropically. The values of ΔG^0 at 920 K and the equilibrium constants ($K = \exp[-\Delta G^0/RT]$) for this reaction are also given in Table 3. In the case of silica-100 and silica-111 surfaces, the formation of mono-oxo species is clearly favored since the equilibrium constants are large. During the oxidation of CH_4 by O_2 the concentration of H_2O in gas phase is typically less than 1% and the total pressure of the reactor is around 1 atm.³⁴ Thus, if the H_2O partial pressure is assumed to be 0.01 atm and the equilibrium constant for the 4-Si ring model given in Table 3 is used, the ratio of mono-oxo to di-oxo is calculated to be 3.8. Significantly higher ratios of mono-oxo to di-oxo species are calculated for the silica-100 and silica-111 models. Thus, the calculated values of K indicate that mono-oxo and di-oxo species can exist in equilibrium with each other, the distribution between the two forms depending on the structure of the silica site to which the molybdate is bonded, the temperature, and the partial pressure of water.

It is known that at temperatures above 773 K silanol groups on the surface of silica can condense releasing water molecules and forming rings containing two silicon atoms and two oxygen atoms.^{39,40} Such two-membered (2M) silicon rings are considered metastable and, hence, are expected to be found only at high temperatures (> 773 K).^{40,41} In the analysis above, it was assumed that silanol groups are present on the surface of silica as illustrated by structure **G** in Figure 2. As the temperature is increased above 773 K a water molecule will be released from such a species leading to a 2M ring on the surface. A model of the di-oxo species with the 2M ring is represented by structure **H** in Figure 2. The energy changes and equilibrium constants for forming such species starting from a mono-oxo species are shown in Table 5. The generic reaction can be represented as



Reaction 2

In the case of the 4-Si ring model, this reaction corresponds to the conversion of structure **F** to structure **H** (see Figure 2).

TABLE 6: Calculated IR and Raman Frequencies for Isolated Molybdate Species Attached to a 4-Si Ring^a (Structures **F** and **G** in Figure 2)

	frequency, cm^{-1}	IR intensity, km/mol	Raman activity, $\text{\AA}^4/\text{amu}$
$(\text{O}=\text{Mo}=\text{O})_{\text{asym}}$	977 (967,970)	62	13
$(\text{O}=\text{Mo}=\text{O})_{\text{sym}}$	995 (993,991)	77	38
$(\text{Mo}=\text{O})$	1014 (1017,1017)	2	45
$(-\text{O}-\text{Mo}=\text{O})$	986 (988,980)	466	7

^a The frequencies for silica-100 and silica-111 models are shown in brackets. The first two rows are for di-oxo models, and the last two rows are for the mono-oxo models.

The corresponding structures on the silica-100 and silica-111 models are given in the Supporting Information. The equilibrium constants given in Table 5 indicate that at 920 K the conversion of a mono-oxo species to a di-oxo species with a 2M ring is an equilibrium process.

Based on the results presented in Tables 3 and 5, one would expect to find both the mono-oxo and the di-oxo species on the surface of amorphous silica, the distribution of these species depending strongly on the local structure of the silica, the temperature, and the partial pressure of water vapor. At 920 K, MoO_x bonded to silica-111 and silica-100 surface structures is predicted to exist primarily as di-oxo species even for very low concentrations of water vapor because of the high equilibrium constants for reactions 1 and 2. However, for MoO_x bonded to 4-silica ring structures, both mono- and di-oxo species are expected to be present, depending on the partial pressure of water vapor.

Vibrational Frequencies of Isolated Silica-Supported MoO_x Species. The vibrational frequencies of $\text{Mo}=\text{O}$ and $\text{O}=\text{Mo}=\text{O}$ stretching modes calculated by DFT for the 4-Si ring model are given in Table 6. The predicted infrared and Raman intensities are also given. The corresponding vibrational frequencies for the silica-100 and silica-111 models are presented in this table as well. In all cases (except $\text{O}=\text{Mo}=\text{O}_{\text{asym}}$ stretch), the corresponding frequencies were found to be within $\pm 4\text{cm}^{-1}$ of the frequencies observed for the 4-Si ring model. In the case of $\text{O}=\text{Mo}=\text{O}_{\text{asym}}$ stretching vibrations, the calculated frequencies are within $\pm 5\text{cm}^{-1}$ of the average value. It is noted, as well, that removing the surface silanol groups (i.e., converting structure **G–H** in Figure 2) does not affect the di-oxo stretching frequencies. The fact that the vibrational frequencies and bond-lengths (Table 4) are relatively insensitive to the surface models used further increases our confidence in the surface models used in this study. Comparison of the vibrational frequencies for mono-oxo and di-oxo structures leads to the following observations: (1) the mono-oxo stretching frequency is generally higher than the di-oxo stretching frequencies and (2) two frequencies separated by 20cm^{-1} , corresponding to the symmetric and asymmetric vibrations of $\text{O}=\text{Mo}=\text{O}$, are observed for the di-oxo species. It is further noted that the mono-oxo species exhibit a $\text{Mo}-\text{O}-\text{Si}$ stretching frequency that is very close to that for $\text{Mo}=\text{O}$ vibrations. The mixing of these vibrational modes produce a new mode with a frequency slightly smaller than that for $\text{Mo}=\text{O}$ stretching vibrations, which is represented as $-\text{O}-\text{Mo}=\text{O}$ in Table 6. This feature is predicted to be most intense in the infrared spectrum of silica-supported MoO_x and to be least intense in the Raman spectrum of such species.

Comparison with Experimental Results. As noted in the Introduction, experimental studies of highly dispersed molybdena on silica have not led to a conclusive view as to whether molybdena in its dehydrated state exists as a mono-oxo or a

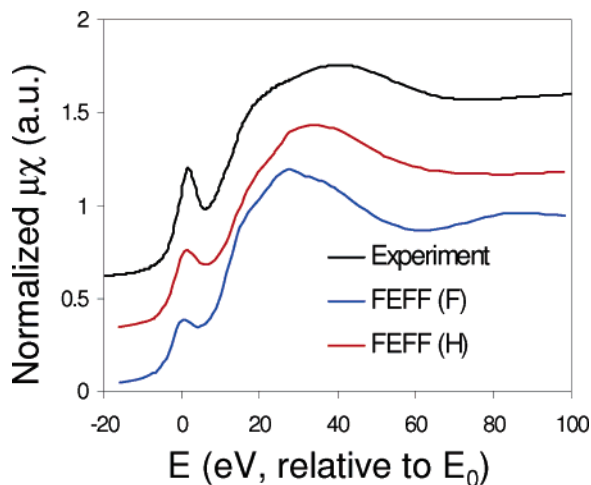


Figure 3. Comparison of experimentally obtained XANES spectrum of $\text{Mo}^{\text{VI}}\text{O}_x/\text{SiO}_x$ with the simulated spectrum for Mo^{VI} in structures **F** (mono-oxo) and **H** (di-oxo).

di-oxo species. For this reason, it was of interest to simulate the XANES and EXAFS patterns, and the Raman spectrum for the mono-oxo and di-oxo species predicted in the present study and to compare these simulated observables with those seen experimentally by Ohler and Bell.²⁷

The FEFF 8^{42,43} software package was used to simulate the XANES and EXAFS spectra for the mono-oxo and di-oxo models. Geometries obtained from the DFT calculations were used as input into the FEFF 8 program. Details of EXAFS and XANES simulations are given in the Supporting Information. Figure 3 shows simulated XANES spectra for the mono-oxo and di-oxo structures, **F** and **H**, respectively, and the experimental XANES spectrum of a $\text{MoO}_x/\text{SiO}_x$ prepared with a Mo surface density of 0.4 Mo/nm². It is evident that both the position and relative intensity of the pre-edge feature in the XANES spectrum calculated for the di-oxo structure are closer to those observed experimentally than those calculated for the mono-oxo structure. A comparison of calculated and experimentally observed EXAFS patterns is shown in Figure 4. The agreement between the EXAFS pattern calculated for the di-oxo species and that observed experimentally is remarkably close, whereas the EXAFS pattern calculated for the mono-oxo species bears limited similarity to the experimentally observed EXAFS pattern. A further point of note is that the Fourier transform of the experimental EXAFS pattern shown in Figure 4 shows peaks at 1.2 and 1.6 Å. These two peaks are attributed to backscattering from the oxygen atoms in Mo=O and Mo–O bonds. Similarly, there is a smaller peak at 2.8 Å which corresponds to backscattering from the nearest Si atoms. The positions of these peaks as predicted by the FEFF simulations for the di-oxo model match very well with those obtained experimentally. In the case of the mono-oxo model, the scattering from the four Mo–O bonds gives rise to a large peak which is the dominant feature in the simulated spectrum. However, the position of this peak does not match any of the peak positions in the experimental spectrum. These observations further support the argument that the MoO_x species on the surface of amorphous silica have a di-oxo rather than a mono-oxo structure.

Raman spectra of molybdena supported at very low Mo surface coverage show only a single peak for Mo=O stretching vibrations for isolated MoO_x species located at 988 cm⁻¹ with a width at half-maximum of 50 cm⁻¹.^{27,34,44} However, the appearance of a single band does not allow one to conclude whether the observed band is due to mono-oxo or di-oxo species

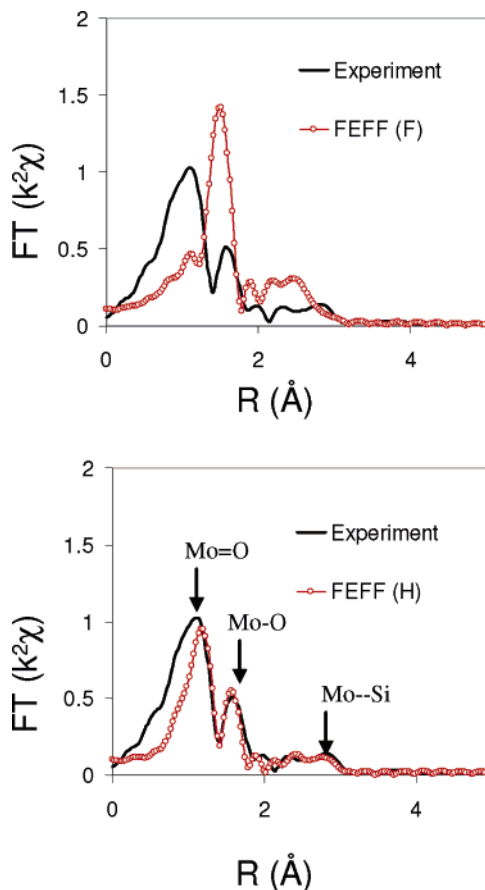


Figure 4. Comparison of experimentally obtained EXAFS spectrum of $\text{Mo}^{\text{VI}}\text{O}_x/\text{SiO}_x$ with the simulated spectrum for Mo^{VI} in structures **F** (mono-oxo) and **H** (di-oxo).

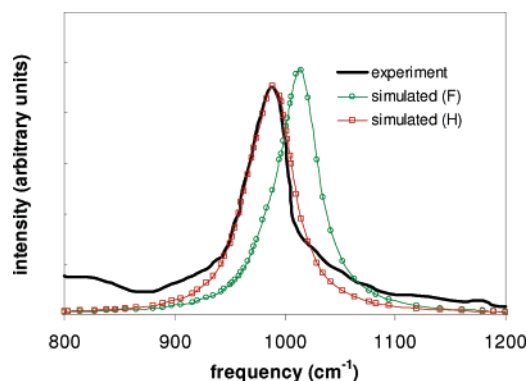
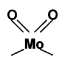
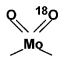
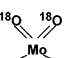
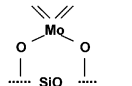
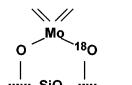
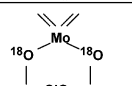
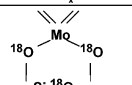


Figure 5. Comparison of the experimentally observed Raman spectrum of $\text{Mo}^{\text{VI}}\text{O}_x/\text{SiO}_x$ with the simulated spectrum for the **F** (mono-oxo) and **H** (di-oxo) models.

or to a combination of the two. Figure 5 shows a simulated Raman spectrum calculated using the data presented in Table 6. Lorentzian functions with a full width at half-maximum of 40 cm⁻¹ were used to simulate the individual peaks, and the height of each simulated spectrum was set to be equivalent to that of the experimentally observed Raman band. The calculated Raman band based on the assumption that only di-oxo species are present agrees very closely with the experimentally observed band. The calculated spectrum for the mono-oxo species gives a peak at around 1014 cm⁻¹, which is 26 cm⁻¹ higher than the experimentally observed peak position.

Ohler and Bell have reported that upon exposure of a calcined sample of $\text{MoO}_x/\text{SiO}_2$ (0.4 Mo/nm²) to H_2^{18}O at 920 K the position of the Raman peak at 988 cm⁻¹ decreased in intensity

TABLE 7: Effects of $^{18}\text{O}/^{16}\text{O}$ Substitution on the Calculated Raman Frequencies for Structure **H**

			
	1) 995 (38) ^a 977 (13) ^b 928 (2) ^c	2) 988 (32) ^d 952 (8) ^e 932 (3) ^c	3) 966 (25) ^a 934 (6) ^b 926 (10) ^c
	4) 993 (29) ^a 977 (14) ^b 911 (2) ^c	5) 988 (24) ^d 951 (11) ^e 910 (4) ^c	6) 960 (28) ^a 935 (7) ^b 928 (12) ^c
	7) 992 (26) ^a 977 (14) ^b 895 (2) ^c	8) 987 (24) ^d 949 (12) ^e 926 (13) ^c	9) 956 (30) ^a 934 (7) ^b 926 (13) ^c
	10) 992 (37) ^a 976 (13) ^b 891 (1) ^c	11) 987 (24) ^d 937 (20) ^e 890 (1) ^c	12) 947 (33) ^a 932 (11) ^b 890 (2) ^c

^a (O=Mo=O) symmetric stretch, where both oxygens have same mass. ^b (O=Mo=O) asymmetric stretch, where both oxygens have same mass. ^c (Mo–O–Si) stretch, where the oxygens are either ^{18}O or ^{16}O . ^d (Mo= ^{16}O) stretch. ^e (Mo= ^{18}O) stretch.

and a new peak appeared at 938 cm^{-1} .²⁷ It was also observed that, after 152 min of exposure to H_2^{18}O , 73% of the ^{16}O atoms on the surface of the silica support were replaced by ^{18}O atoms. These results can now be compared with the vibrational analyses performed on the di-oxo model (**H** in Figure 2) for different levels of $^{18}\text{O}/^{16}\text{O}$ substitution as shown in Table 7. The four rows in this table correspond to cases in which the ^{16}O atoms of Mo–O–Si and Si–O–Si linkages are replaced progressively by ^{18}O atoms. The columns in this table represent different levels of ^{18}O substitution of the O atoms in the Mo=O groups. Three Raman frequencies are reported for each case listed. Each of these modes is comprised of a combination of Mo=O and Mo–O–Si vibrations, the degree of mixing depending on the overall degree of ^{18}O replacement of ^{16}O . The Raman intensity of each band is shown in brackets, and the band with the highest intensity is shown in bold. For case 1, in which all of the O atoms are ^{16}O , the most intense band is that for symmetric O=Mo=O stretching vibrations at 995 cm^{-1} . As discussed above, the convolution of this band with the somewhat weaker band at 977 cm^{-1} for asymmetric O=Mo=O stretching vibrations results in a near perfect representation of the observed Raman band (see Figure 5) for $\text{MoO}_x/\text{SiO}_2$ calcined at 920 K in O_2 . If all of the O atoms in structure **H** are ^{18}O -labeled (case 12), then the frequency of the most intense band shifts to 947 cm^{-1} . Convolution of this band with the one at 932 cm^{-1} shifts the band center to 945 cm^{-1} , in good agreement with that observed at 938 cm^{-1} following treatment of $\text{MoO}_x/\text{SiO}_2$ by H_2^{18}O at 920 K.

We examine next what happens when the ^{16}O atoms in structure **H** are partially replaced by ^{18}O atoms. Progressive substitution of ^{18}O for ^{16}O in the Mo–O–Si and Si–O–Si bonds of **H** (cases 1, 4, 7, and 10) has little effect on the positions of the most intense band, which occurs at 995–992 cm^{-1} , and has no effect of the position of the second most intense band at 977 cm^{-1} . When ^{18}O is substituted for ^{16}O in one of the two Mo=O bonds of **H** (cases 2, 5, 8, and 11), the position of the most intense band red shifts by no more than 5–7 cm^{-1} relative to the case where both Mo=O bonds in **H** are ^{16}O -labeled. Table 7 shows that a significant shift in the position of the most intense Raman band occurs only when both Mo=O bonds become ^{18}O -labeled (cases 3, 6, 9, and 12), the

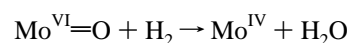
TABLE 8: Calculated Values of ΔE and $\Delta G^0(920)$ for the Reduction of Mo^{VI} to Mo^{IV}

reactant/product ^a	surface	ΔE , kcal/mol	$\Delta G^0(920)$, kcal/mol
F/I	4-Si ring	22.7	14.2
F/I	Silica–100	20.2	10.6
F/I	Silica–111	23.0	14.1
H/J	4-Si ring	14.3	6.6

^a The structures of the reactants **F** and **H** and products **I** and **J** are given in Figure 2 and in the Supporting Information.

degree of the red shift depending on the degree to which the Mo–O–Si and Si–O–Si bonds are ^{18}O labeled. These results suggest that it would be hard to observe the partial substitution of ^{16}O by ^{18}O in di-oxo structures, such as **H**. Further complicating the matter is the recognition that experimentally observed Raman line widths are of the order of 40 cm^{-1} . It should also be recognized that the sequence in which ^{18}O is introduced into Mo=O, Mo–O–Mo, and Si–O–Si bonds cannot be controlled, and consequently only the species that are fully ^{16}O or ^{18}O will be clearly recognized. Therefore, failure to observe Raman or infrared bands associated with the intermediate levels of ^{18}O exchange is not surprising and cannot be used to argue against the existence of a di-oxo structure.

Reducibility of Isolated MoO_x Species. The reduction of isolated Mo^{VI} oxo species was also investigated in order to determine the Gibbs free energy for this process and the structure of the reduced Mo^{IV} oxo species. This effort was stimulated by the work of Ohler and Bell,²⁷ which showed that isolated Mo^{VI} oxo species can be reduced completely to isolated Mo^{IV} species by reaction with 1 atm of flowing H_2 at 920 K. Reduction resulted in the loss of the Raman band for Mo=O vibrations, whereas reoxidation of the reduced species with O_2 showed that one O atom per Mo atom had been removed upon reduction. These results suggest the following reaction occurred during reduction:



Species **I** in Figure 2 represents an isolated Mo^{IV} species formed by the reduction of mono-oxo species, **F**. There are four Mo–O bonds of length 1.92 Å, and there are no terminal Mo=O bonds. Table 8 shows the calculated values of ΔE and ΔG^0 evaluated at 920 K for the reduction of Mo^{VI} to Mo^{IV} for different models of the silica surface. The first three rows of Table 8 show that the values ΔE are within ± 1.5 kcal/mol of each other for the different models of the silica surface, indicating that the thermodynamics for the reduction of Mo^{VI} oxo species are relatively insensitive to the model used to represent the silica surface. Since our analysis of Mo^{VI} species show that di-oxo species are favored, we calculated the thermodynamics for reducing a di-oxo Mo^{VI} to a Mo^{IV} species (**H** to **J** in Figure 2). The product of the reaction has one terminal Mo=O bond of length 1.70 Å and two Mo–O bonds of length 2.00 Å. The triplet state is more stable than the singlet state for this structure by 16.6 kcal/mol. In the case of structure **I**, the singlet state was stable by 18.0 kcal/mol. The thermodynamics reported in Table 8 are calculated using the energy for the most stable electronic states (i.e., triplet state for structure **J** and singlet state for structure **I**). The reduction of **H** to **J** is characterized by $\Delta E = 14.3$ kcal/mol and $\Delta G^0 = 6.6$ kcal/mol.

Ohler and Bell²⁷ have reported that the reduction of isolated Mo^{VI} molybdate species supported on silica in 1 atm of H_2 at 920 K resulted in a considerable loss in the intensity of the band at 988 cm^{-1} . This may suggest that either the reduction

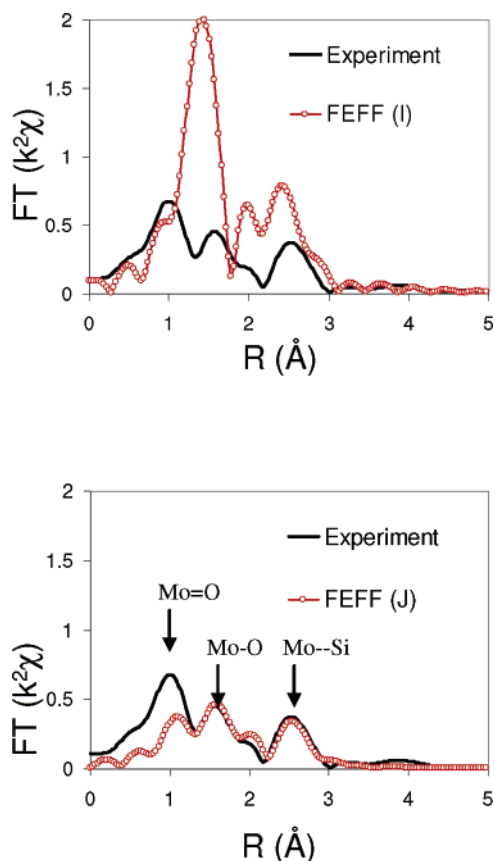


Figure 6. Comparison of experimentally obtained EXAFS spectrum of $\text{Mo}^{\text{IV}}\text{O}_x/\text{SiO}_x$ with the simulated spectrum for Mo^{IV} in structures **I** and **J**.

of Mo^{VI} is not complete or that the resulting Mo^{IV} species also has a Raman band at around 988 cm^{-1} . Our DFT calculations show that **J**, which has one $\text{Mo}=\text{O}$ bond, has a Raman band at 995 cm^{-1} with an intensity of $14\text{ \AA}^4/\text{amu}$. This intensity is $1/3$ of that for the $\text{Mo}=\text{O}$ vibrations in **H** which are calculated to be at 995 cm^{-1} . This suggests that the loss in intensity observed when highly dispersed $\text{MoO}_x/\text{SiO}_2$ is reduced in H_2 at 920 K is due to the conversion of **H** to **J**.

Further support for **J** being the correct representation of isolated Mo^{VI} centers supported on silica comes from a comparison of the theoretically generated EXAFS pattern with that obtained experimentally. Figure 6 compares the simulated EXAFS patterns for **I** and **J** with that seen experimentally following the reduction of highly dispersed $\text{MoO}_x/\text{SiO}_2$ in 1 atm H_2 at 920 K . The simulated EXAFS pattern for **J** agrees closely with the experimental EXAFS pattern, but that for **I** does not. These results indicate strongly that upon reduction **H** is converted to **J**.

The value of ΔG^0 given in Table 8 for the reduction of **H** to **J** can be used to evaluate the equilibrium constant for this process and, in turn, the extent of reduction for a given set of H_2 and H_2O partial pressures, P_{H_2} and $P_{\text{H}_2\text{O}}$, respectively. At equilibrium, the fraction of Mo^{IV} to Mo^{VI} will then be given by

$$\frac{\theta_{\text{IV}}}{\theta_{\text{VI}}} = K_{\text{eq}} \frac{P_{\text{H}_2}}{P_{\text{H}_2\text{O}}} \quad (1)$$

where θ_{IV} and θ_{VI} are the mole fractions of Mo^{IV} and Mo^{VI} respectively and K_{eq} is the equilibrium constant at 920 K . For the di-oxo model on 4-Si ring, **H**, K_{eq} has a value of $2.7 \times$

10^{-2} . Thus, if $P_{\text{H}_2} = 1\text{ atm}$ then $P_{\text{H}_2\text{O}}$ would need to be equal to $<10^{-4}\text{ atm}$ for $\theta_{\text{IV}}/\theta_{\text{VI}} > 10^2$. The requisite level of water vapor is quite reasonable for the experiments described by Ohler and Bell.²⁷

Conclusions

The structure and vibrational properties of isolated molybdate species bonded to the surface of amorphous silica have been determined from DFT calculations. It is shown that silica-supported molybdates can exist as mono-oxo and di-oxo structures in equilibrium with each other, the distribution between the two structural types depending on the temperature, partial pressure of water, and the structure of the silica at the point of molybdate attachment. The simulated EXAFS patterns of mono-oxo and di-oxo structures are quite different. On the other hand, the calculated Raman spectra of these structures exhibit bands in the range of $992 \pm 22\text{ cm}^{-1}$, making it hard to differentiate between the mono-oxo and di-oxo species based purely on Raman spectroscopy. Comparison of experimentally observed XANES, EXAFS, and Raman data obtained for isolated molybdate species supported on silica following calcination at 920 K with similar results calculated for mono-oxo and di-oxo species strongly supports the conclusion that isolated Mo^{VI} molybdate species on silica exist as di-oxo species (structure **H** in Figure 2). The calculated Gibbs free energy for the reduction of isolated molybdate species from Mo^{IV} to Mo^{IV} in H_2 is relatively insensitive to the model of the silica surface used, and the extent of molybdate reduction determined for reduction in H_2 at 920 K is consistent with that observed experimentally. Comparison of the predicted and experimentally observed Raman spectrum and the EXAFS pattern of reduced MoO_x species supported on silica strongly suggests that such Mo^{IV} species are present as mono-oxo species (structure **J** in Figure 2).

Acknowledgment. This work was supported by the Methane Conversion Cooperative funded by BP.

Supporting Information Available: Figures of the MoO_x species on silica-111 model and silica-100 model and details of the FEFF 8.0 simulations are given in a PDF file. Energies and coordinates of all structures are deposited in EXCEL and XYZ formats. This material is available free of charge via the Internet at <http://pubs.acs.org>.

References and Notes

- (1) Vikulov, K. A.; Elev, I. V.; Shelimov, B. N.; Kazansky, V. B. *J. Mol. Catal.* **1989**, *55*, 126.
- (2) Handzlik, J. *J. Phys. Chem. B* **2005**, *109*, 20794.
- (3) Jehng, J. M.; Hu, H. C.; Gao, X. T.; Wachs, I. E. *Catal. Today* **1996**, *28*, 335.
- (4) Liu, H. C.; Iglesia, E. *J. Catal.* **2002**, *208*, 1.
- (5) Pitchai, R.; Klier, K. *Catal. Rev.—Sci. Eng.* **1986**, *28*, 13.
- (6) Chen, K. D.; Bell, A. T.; Iglesia, E. *J. Catal.* **2002**, *209*, 35.
- (7) Biermann, J. J. P.; Janssen, F.; Ross, J. R. H. *Appl. Catal., A* **1992**, *86*, 165.
- (8) Lietti, L.; Ramis, G.; Busca, G.; Bregani, F.; Forzatti, P. *Catal. Today* **2000**, *61*, 187.
- (9) Nova, I.; Lietti, L.; Casagrande, L.; Dall'Acqua, L.; Giamello, E.; Forzatti, P. *Appl. Catal., B* **1998**, *17*, 245.
- (10) Banares, M. A.; Wachs, I. E. *J. Raman Spectrosc.* **2002**, *33*, 359.
- (11) Ono, T.; Kamisuki, H.; Hisashi, H.; Miyata, H. *J. Catal.* **1989**, *116*, 303.
- (12) Mestl, G.; Srinivasan, T. K. *Catal. Rev.—Sci. Eng.* **1998**, *40*, 451.
- (13) Anpo, M.; Kondo, M.; Coluccia, S.; Louis, C.; Che, M. *J. Am. Chem. Soc.* **1989**, *111*, 8791.
- (14) Arena, F.; Parmaliana, A. *Acc. Chem. Res.* **2003**, *36*, 867.
- (15) Cornac, M.; Janin, A.; Lavalley, J. C. *Polyhedron* **1986**, *5*, 183.

- (16) Deboer, M.; Vandillen, A. J.; Koningsberger, D. C.; Geus, J. W.; Vuurman, M. A.; Wachs, I. E. *Catal. Lett.* **1991**, *11*, 227.
- (17) Hu, H. C.; Wachs, I. E.; Bare, S. R. *J. Phys. Chem.* **1995**, *99*, 10897.
- (18) Iwasawa, Y.; Ogasawara, S. *J. Chem. Soc., Faraday Trans.* **1979**, *75*, 1465.
- (19) Radhakrishnan, R.; Reed, C.; Oyama, S. T.; Seman, M.; Kondo, J. N.; Domen, K.; Ohminami, Y.; Asakura, K. *J. Phys. Chem. B* **2001**, *105*, 8519.
- (20) Shelimov, B. N.; Pershin, A. N.; Kazansky, V. B. *J. Catal.* **1980**, *64*, 426.
- (21) Takenaka, S.; Tanaka, T.; Funabiki, T.; Yoshida, S. *J. Phys. Chem. B* **1998**, *102*, 2960.
- (22) Iijima, K. *Bull. Chem. Soc. Jpn.* **1977**, *50*, 373.
- (23) Thomassen, H.; Hedberg, K. *J. Mol. Struct.* **1992**, *273*, 197.
- (24) Jarupatrakorn, J.; Coles, M. P.; Tilley, T. D. *Chem. Mater.* **2005**, *17*, 1818.
- (25) Banares, M. A.; Hu, H. C.; Wachs, I. E. *J. Catal.* **1994**, *150*, 407.
- (26) Desikan, A. N.; Huang, L.; Oyama, S. T. *J. Chem. Soc., Faraday Trans.* **1992**, *88*, 3357.
- (27) Ohler, N.; Bell, A. T. *J. Phys. Chem. B* **2005**, *109*, 23419.
- (28) Fu, G.; Xu, X.; Lu, X.; Wan, H. L. *J. Phys. Chem. B* **2005**, *109*, 6416.
- (29) Fu, G.; Xu, X.; Lu, X.; Wan, H. L. *J. Am. Chem. Soc.* **2005**, *127*, 3989.
- (30) Frisch, M. J.; Trucks, G. W.; Schlegel, H. B.; Scuseria, G. E.; Robb, M. A.; Cheeseman, J. R.; Montgomery, Jr., J. A.; Vreven, T.; Kudin, K. N.; Burant, J. C.; Millam, J. M.; Iyengar, S. S.; Tomasi, J.; Barone, V.; Mennucci, B.; Cossi, M.; Scalmani, G.; Rega, N.; Petersson, G. A.; Nakatsuji, H.; Hada, M.; Ehara, M.; Toyota, K.; Fukuda, R.; Hasegawa, J.; Ishida, M.; Nakajima, T.; Honda, Y.; Kitao, O.; Nakai, H.; Klene, M.; Li, X.; Knox, J. E.; Hratchian, H. P.; Cross, J. B.; Bakken, V.; Adamo, C.; Jaramillo, J.; Gomperts, R.; Stratmann, R. E.; Yazyev, O.; Austin, A. J.; Cammi, R.; Pomelli, C.; Ochterski, J. W.; Ayala, P. Y.; Morokuma, K.; Voth, G. A.; Salvador, P.; Dannenberg, J. J.; Zakrzewski, V. G.; Dapprich, S.; Daniels, A. D.; Strain, M. C.; Farkas, O.; Malick, D. K.; Rabuck, A. D.; Raghavachari, K.; Foresman, J. B.; Ortiz, J. V.; Cui, Q.; Baboul, A. G.; Clifford, S.; Cioslowski, J.; Stefanov, B. B.; Liu, G.; Liashenko, A.; Piskorz, P.; Komaromi, I.; Martin, R. L.; Fox, D. J.; Keith, T.; Al-Laham, M. A.; Peng, C. Y.; Nanayakkara, A.; Challacombe, M.; Gill, P. M. W.; Johnson, B.; Chen, W.; Wong, M. W.; Gonzalez, C.; Pople, J. A. *Gaussian 03*, revision C.02; Gaussian, Inc.: Wallingford, CT, 2004.
- (31) Wong, M. W. *Chem. Phys. Lett.* **1996**, *256*, 391.
- (32) Schaftenaar, G.; Noordik, J. H. *J. Comput. Aided Mol. Des.* **2000**, *14*, 123.
- (33) Jaguar, 5.5 ed.; Schrödinger, LLC: Portland, OR, 2003.
- (34) Ohler, N.; Bell, A. T. *J. Catal.* **2005**, *231*, 115.
- (35) Alexander, L. E.; Beattie, I. R.; Bukovszky, A.; Jones, P. J.; Marsden, C. J.; Van Schalkwyk, G. J. *J. Chem. Soc., Dalton Trans.* **1974**, 81.
- (36) Neikirk, D. L.; Fagerli, J. C.; Smith, M. L.; Mosman, D.; Devore, T. C. *J. Mol. Struct.* **1991**, *244*, 165.
- (37) Accelrys. MS Modeling v3.0, 2003. Accelrys Software, Inc.
- (38) Roder, A.; Kob, W.; Binder, K. *J. Chem. Phys.* **2001**, *114*, 7602.
- (39) Iarlori, S.; Ceresoli, D.; Bernasconi, M.; Donadio, D.; Parrinello, M. *J. Phys. Chem. B* **2001**, *105*, 8007.
- (40) Grabbe, A.; Michalske, T. A.; Smith, W. L. *J. Phys. Chem.* **1995**, *99*, 4648.
- (41) Ceresoli, D.; Bernasconi, M.; Iarlori, S.; Parrinello, M.; Tosatti, E. *Phys. Rev. Lett.* **2000**, *84*, 3887.
- (42) Ankudinov, A. L.; Ravel, B.; Rehr, J. J.; Conradson, S. D. *Phys. Rev. B* **1998**, *58*, 7565.
- (43) FEFF 8.0, <http://feff.phys.washington.edu/>.
- (44) Ohler, N.; Bell, A. T. *J. Phys. Chem. B* **2006**, *110*, 2700.